Microwave Stimulation of Energetic Al-Based Nanoparticle Composites for Ignition Modulation

Zaira Alibay, Daniel Olsen, Prithwish Biswas, Cody England, Feiyu Xu, Pankaj Ghildiyal, Min Zhou, and Michael R. Zachariah*

Cite This: *ACS Appl. Nano Mater.* 2022, 5, 2460−2469

Read Online

ACCESS | Metrics & More | Article Recommendations | Supporting Information

ABSTRACT: Although electromagnetic stimulation promises safe and controlled ignition of energetic materials, ultraviolet (UV) to infrared (IR) wavelength sources experience significant photon attenuations in energetic materials. Conversely, radiation in microwave frequencies is recognized for instantaneous volumetric heating capabilities. However, many energetics are poor microwave heaters, and to accelerate the heating, recent efforts focused on adding microwave susceptors that do not participate in the energetic reaction. This is the first effort to demonstrate that nanoscale aluminum (nAl)/manganese oxide (MnO_x) can be rapidly heated at rates $\sim10^4$ °C/s under microwave radiation without addition of inert microwave susceptors. Detailed analysis of nanoscale MnO_x was performed via X-ray photoelectron spectroscopy (XPS), X-ray diffraction (XRD), and transmission electron microscopy (TEM). The samples of MnO_x at different loadings of nAl were three-dimensionally (3D) printed into composite films and tested with a microwave applicator at a 2.45 GHz frequency. Infrared thermometry experiments showed that with an increase in MnO_x content the heating rate in the samples increases by orders of magnitude. Computational modeling based on the dielectric and thermophysical properties of the materials showed that an electric field is the dominant mechanism accounting for $\sim96\%$ of the heating of the nAl/MnO_x composites at microwave frequencies. The microwave ignition mechanism was deconvoluted via high-speed IR imaging, in situ time-of-flight mass spectroscopy (TOFMS), temperature-jump (T-jump), and thermogravimetric analysis/differential scanning calorimetry (TGA/DSC) analysis. The results show that microwave stimulation can effectively heat and control ignition in nAl-based thermites with MnO_x, where the oxidizer acts dually as a microwave susceptor and an ignition driver.

KEYWORDS: *manganese oxide, nanoaluminum, microwave heating, electromagnetic, energetic nanocomposites*
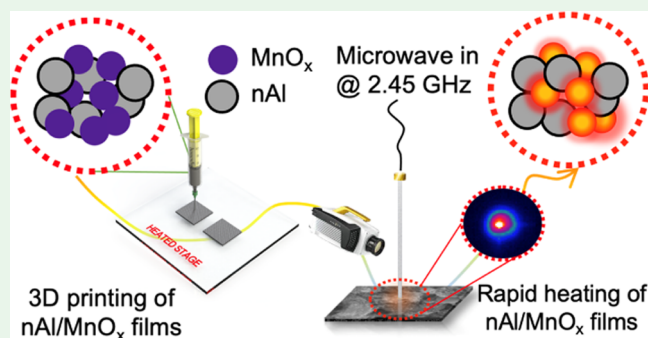
1. INTRODUCTION

With uses spanning from microchip initiators to automobile safety airbags, energetic materials have found applications in both military and civilian industries. Nanoscale heterogeneous energetic materials have been of particular interest due to their high energy density, environmental benignancy, and tunability.[1−5] Although successfully employed, safe and controlled ignition of solid propellants as well as dynamic modulation of their energy release rates is a challenge.[6] One way of addressing this challenge has been through the assembly and additive manufacturing of nanoscale thermites with tunable energy release rates during combustion.[7−9] Along this path, electromagnetic (EM) stimulation via laser or flash ignition[10−12] has been used as a means of safe ignition. In this regard, ultraviolet (UV) to infrared (IR) frequencies have been widely explored for ignition; however, the associated high photon attenuation in energetic materials has limited the complete exploitation of the propellant volume.[13−16] Uhlenhake et al. showed that the absorbed energy in nAl

(nanoaluminum)/poly(vinylidene fluoride) (PVDF) energetic composite films, at a 10 wt % loading, diminishes within a ~4 μm depth, indicating that the UV−IR wavelength ignition sources primarily rely on surface heating effects.[17] To address this challenge, one could extend the incident wavelength to microwave frequencies: 300 MHz to 3000 GHz.

Unlike UV, visible, and IR radiation, microwave wavelengths are low energy and capable of penetrating deep into the material volume. Microwave radiation incident on a material can lead to dielectric heating, arc discharge, and ionization of the gaseous species, which in turn can be employed to modulate combustion performance.[18,19] Dielectric heating is
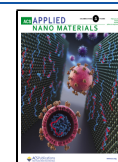
expected to be the initiator to thermally driven reactions and would occur before gaseous species are released. This dielectric heating is expected to be a primary contributor in overcoming the reaction activation barrier and regulating the ignition event.[20] Research on microwave stimulation of metal particles (often used as fuels) have demonstrated that the dielectric (native oxide) coating on metals can dramatically increase electromagnetic (EM) absorption in otherwise microwave insensitive particles.[21,22] This led to the design of architectures where nTi coated with TiO_2/TiN was used to stimulate microwave ignition in energetic materials.[23]

On the other hand, aluminum is nominally the fuel of choice due to its relatively low cost and mass and volume specific energy density.[24−28] However, the dielectric properties of nAl render it relatively microwave insensitive.[23,29] Thermites of nAl/Fe_3O_4 previously studied under microwave stimulation show that while initiation can be obtained, the event extended to several minutes.[30] To compensate for the microwave passiveness of nAl, sensitizers, such as graphene, carbon nanotubes, and reduced graphene oxide (rGO), have been added to energetic materials[29,31,32] to ignite and modulate combustion via microwave radiation. Since these materials do not participate in the energetic reaction, the increase in the microwave sensitivity decreases the exothermic output of the composites. This finding led to our exploration of metal oxides that are capable of harnessing the energy density of nAl while being microwave sensitive. The manganese dioxide (MnO_2) reaction with nAl has been previously studied[33−35] and the theoretical heat release from the thermite reaction of MnO_2 and Al is higher or comparable to classical thermites of Al/Fe_3O_4 and Al/CuO.[27] Moreover, multivalent manganese oxides (−3 to +7 oxidation states) have been shown to have high dielectric constant values and have been utilized in microwave-assisted catalysis applications.[36−41] The dielectric properties of the oxidizer open avenues for exploration of the metal oxide in nAl-based microwave-stimulated thermites.

In this work, we investigate the microwave heating and ignition mechanism of nanoscale Al/MnO_x energetic composites. We study the heating rates of MnO_x composites via infrared thermometry and primary heating mechanisms via finite element simulations under incident microwaves at 2.45 GHz. The detailed analysis of the MnO_x nanopowder composition was performed via X-ray diffraction (XRD), X-ray photoelectron spectroscopy (XPS), and thermogravimetric analysis (TGA) techniques. The morphologies of the as-received MnO_2/Mn_2O_3 nanopowders as well as of direct-ink written films were characterized with scanning electron and transmission electron microscopy (SEM and TEM). Commercially available mixtures of MnO_2/Mn_2O_3 were formulated with nAl at different equivalence ratios to better understand the range of microwave ignition of nAl-based thermites. In situ temperature-jump ignition (T-jump), time-of-flight mass spectroscopy (TOFMS), and differential scanning calorimetry (DSC) were used to uncover the thermochemical reactions in the three-dimensional (3D) printed energetic composites and shed a light on the ignition mechanism. This paper demonstrates that MnO_x is an excellent oxidizer for microwave ignition with nAl and not only drives the heating of the energetic composites under microwave stimulation but also controls the ignition in the 3D printed nAl/MnO_x films.

2. MATERIAL AND METHODS

2.1. Materials and Sample Preparation. Manganese dioxide (MnO_2, 50−80 nm) and aluminum nanoparticles (nAl, 80 nm) were purchased from US Research Nanomaterials, Inc. and Novacentrix, respectively. Thermogravimetric analysis showed that nAl has 77% active metal content by mass, which was considered in all stoichiometric calculations of nAl/MnO_x formulations. Methylcellulose (HPMC, METHOCEL F4M) with a molecular weight of 86 000 was purchased from DuPont. Poly(vinylidene fluoride) (PVDF, average molecular weight: ∼534 000) and N,N-dimethylformamide (DMF, 99.8%) were purchased from Sigma-Aldrich. All materials were used as received with no further treatment.

A polymer base for the high loading solid inks was first prepared by dissolving PVDF and HPMC at the 2/3 mass ratio in DMF with a total polymer concentration of 31.25 mg/mL. The polymer solution was magnetically stirred for a minimum of 2 h. Nanopowder was then added to the clear solution and lightly vortexed and sonicated for 30 min in a Branson sonicator. The vortexing and sonication steps were repeated after each new addition of a constituent. After all components were added, the ink was magnetically stirred for 24 h and mechanically mixed for 1.5 h prior to fabrication by 3D printing.

2.2. 3D Printed Film Fabrication. The prepared ink was transferred to a 10 mL Beckman Colder syringe with a 16-gauge needle tip (1.6 mm ID) and printed on a hot bed via direct-ink writing method on a Hyrel 3D printer. The temperature of the hot bed was maintained at 70 °C to allow evaporation of the DMF as the film layers were printed. The inks were printed at 250 mm/min with the extrusion rate of 56.3 mm³/min and a total of two layers were printed for all ink formulations.

2.3. Morphology and Thermochemistry Characterization. X-ray photoelectron spectroscopy (XPS) characterization was carried out using a Kratos AXIS ULTRA^DLD XPS system equipped with an Al Kα X-ray source and a 165 mm mean radius electron energy hemispherical analyzer. The as-received MnO_x nanopowder and microstructures of the printed samples were investigated with a ThermoFisher Scientific NNS450 scanning electron microscope (SEM) and transmission electron microscope (TEM) Talos L120C. Powder X-ray diffraction (XRD, PANalytical Empyrean Series 2, Cu Kα source (λ = 1.543 Å)) was employed to analyze MnO_x nanopowder and $Al/MnO_x/HPMC/PVDF$ reaction post-products in air with a step size of 0.013°.

Interactions of the fabricated film with air, as well as interactions of MnO_x with nAl in the PVDF/HPMC matrix, were investigated with simultaneous thermogravimetry−differential scanning calorimetry (TGA−DSC) (STA 449 F3 Jupiter, NETZCSH). The samples were heated at a rate of 10 K/min from 25 to 1000 °C in air and under an argon flow rate of 70 mL/min. Masses of 1−3 mg were loaded per TGA−DSC run.

2.4. Microwave Emitter Configuration. A spatially localized microwave emitter apparatus has been employed for all microwave heating tests with the infrared camera and is described in more detail elsewhere.[33] The emitter configuration includes a solid-state micro-wave generator (DS Instruments SG12000) with a peak power output of 10 dBm at 2.45 GHz, as seen in Figure 1. The output signal from the generator is then amplified by a solid-state amplifier with the peak gain of 32 dB, allowing the output power to be maximized to 42 dBm (∼15 W). The output signal is transmitted through a coaxial cable terminated with a nickel-plated straight pin (Singer 0.025″ diameter, mm length) mounted on a custom-made brass adapter. The sample to antenna distance was controlled via a micrometer-precision translational stage, where the antenna tip was placed directly in contact with the sample without penetrating the material, as seen in Figure 1.

2.5. Thermal Imaging Characterization. A Telops FASTM3K infrared (IR) camera was used to measure surface temperature at 10 000−20 000 frames per second during microwave irradiation. A 50 mm lens with a 1 inch extender ring was attached to the camera (In/Sb detector) and a fixed exposure of 5 μs was used on all acquired images. The camera was set to a temperature range of 0−151 °C per calibration range of the device. The heating rates were calculated as
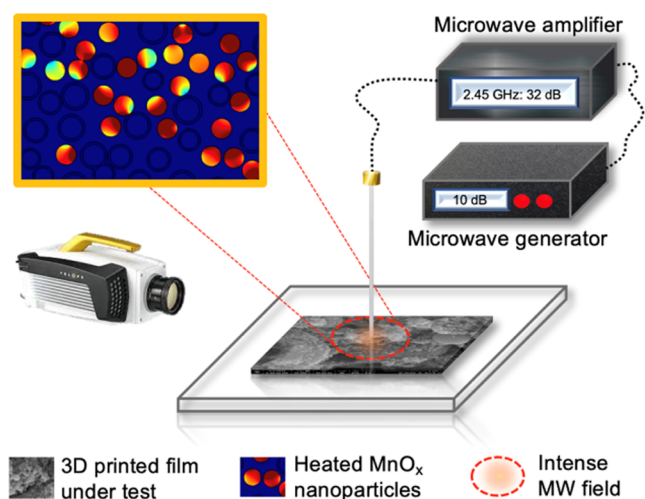
Figure 1. Schematic illustration of the microwave emitter configuration.

slopes of the temperature vs time curves. The pixel pitch of the camera detector was 30 μm and the temperature was averaged over 75 μm region when the lens was situated 268 mm away from the sample.

2.6. Modeling/Simulations. Along with the experimental studies, computational analyses of the microwave heating of the MnO_x and nAl/MnO_x in the PVDF matrix were carried out. The primary intent is to understand how heating occurs through the interactions of the electric and magnetic fields (E-field and H-field, respectively) of the incident microwaves with the composite microstructures of both dielectric and conducting constituents. To this end, the microstructure models include four constituents: PVDF, aluminum oxide (Al_2O_3), aluminum (Al), and MnO_x. HPMC was not included in the matrix as the polymer's thermophysical properties are similar to that of PVDF. Particles in the microstructure have radii of between 25 and 35 nm for aluminum and only 25 nm for MnO_x. The thickness of the oxide shell around each aluminum particle is such that the active aluminum core is 77 wt %, matching that for the nAl used experimentally. The core–shell structured particles are embedded in the PVDF binder matrix. The microstructures were used in electrodynamic calculations, which track the E-fields and the H-fields through which dielectric heating and conductive heating are evaluated. The material properties used in the modeling are presented in Table 1.

The calculations were carried out in COMSOL Multiphysics.[42] The microstructure samples are 3 μm × 8 μm in size. This size is smaller than the 2 mm × 2 mm × 250 μm sample size used in the experiments, as necessitated by high computational costs for larger samples. Even so, the model allows the mechanisms and extent of heating to be analyzed. This computationally efficient model probes the scattering and absorption of the incident energy by the particles and the binder in the microstructures. To match the experiments, multiple samples with different amounts of nAl and MnO_x were created. The particles are approximately uniformly distributed in the microstructures; particulate agglomeration and voids were not modeled. The excitation condition emulates that in the experiments, with the incident wave coming from the top of the two-dimensional

sample and the E-field vector in plane and horizontal. The symmetrical boundary conditions were applied at the edges of the 3 μm wide sample, where the incident wave was incident evenly across the top and heat losses to the surrounding were not accounted for. The boundary condition at the bottom edge of the sample was transparent such that EM waves can pass through deeper into the material, thereby accounting for the effect of the larger specimen size in the experiments. The model setup allows the effects of microstructures to be explicitly analyzed.

2.7. T-jump Ignition and Time-of-Flight Mass Spectroscopy. The ignition temperatures of the energetic composites and temporal evolution of O_2 species from MnO_x were measured by T-jump and time-of-flight mass spectroscopy (TOFMS) methods that are described in more detail elsewhere.[49] Briefly, the samples were thinly coated on a Pt wire (length ~0.8 cm, diameter ~76 μm, Omega Engineering, Inc), which was pulse-heated to ~1500 K at ~10^5 K/s in a specialized chamber. The measurements were conducted either under vacuum or an air/argon atmosphere at 1 atm. The temperature of the wire is monitored by probing the current and voltage across the wire at a temporal resolution of 100 ns. The ignition delay time was captured at ~ μs resolution with a high-speed camera (Vision Research Phantom V12.1). The ignition time was defined as a time of first light after which sustained combustion on the wire was observed. The measured ignition timestamps were coupled to the wire temperatures (calculated via the Callendar–Van Dusen equation) to determine the corresponding ignition temperatures.

3. RESULTS

The composition of as-received manganese oxide powder was characterized via X-ray photoelectron spectroscopy (XPS), X-ray diffraction analysis (XRD), and thermogravimetric analysis (TGA). XRD analysis in Figure 2c demonstrated that the metal oxide contains crystalline phase Mn_2O_3. XPS analysis showed that the Mn $2p_{3/2}$ peak of the as-received powder (642.0 eV) is close to that of Mn^{4+} (MnO_2) at 642.1 eV (Figure 2A). The shift to a lower binding energy is indicative of the presence of Mn^{3+}. Further investigation of the splitting of Mn 3s peaks, MnO_2 (ΔE = 4.8 eV), Mn_2O_3 (ΔE = 5.5 eV), and MnO (ΔE = 5.9 eV), has been used to distinguish different oxidation states of manganese oxides.[50−52] In Figure 2A, the splitting of the as-received powder is 5.1 eV, which is between the characteristic values of MnO_2 and Mn_2O_3. These results suggest that as-received MnO_2 nanopowder is in fact an assortment of MnO_2 and Mn_2O_3. The absence of the MnO_2 traces in XRD spectra confirms (Figure 2c) that there is no crystalline phase manganese dioxide present in the as-received powders; however, characteristic $2p_{3/2}$ and 3s traces of MnO_2 in XPS spectra reveal the presence of amorphous phase Mn^{4+} species. To quantitatively analyze the bulk composition of the manganese oxide powder, thermogravimetric analysis was performed in an argon environment. A two-step mass loss under argon flow in the TGA plot of Figure 2d is characteristic of the phase transition of $MnO_2 \rightarrow Mn_2O_3$ at 530 °C (5.4% loss) and $Mn_2O_3 \rightarrow Mn_3O_4$ at 730 °C (3.7% loss).[33,53]

Table 1. Material Properties of Constituents

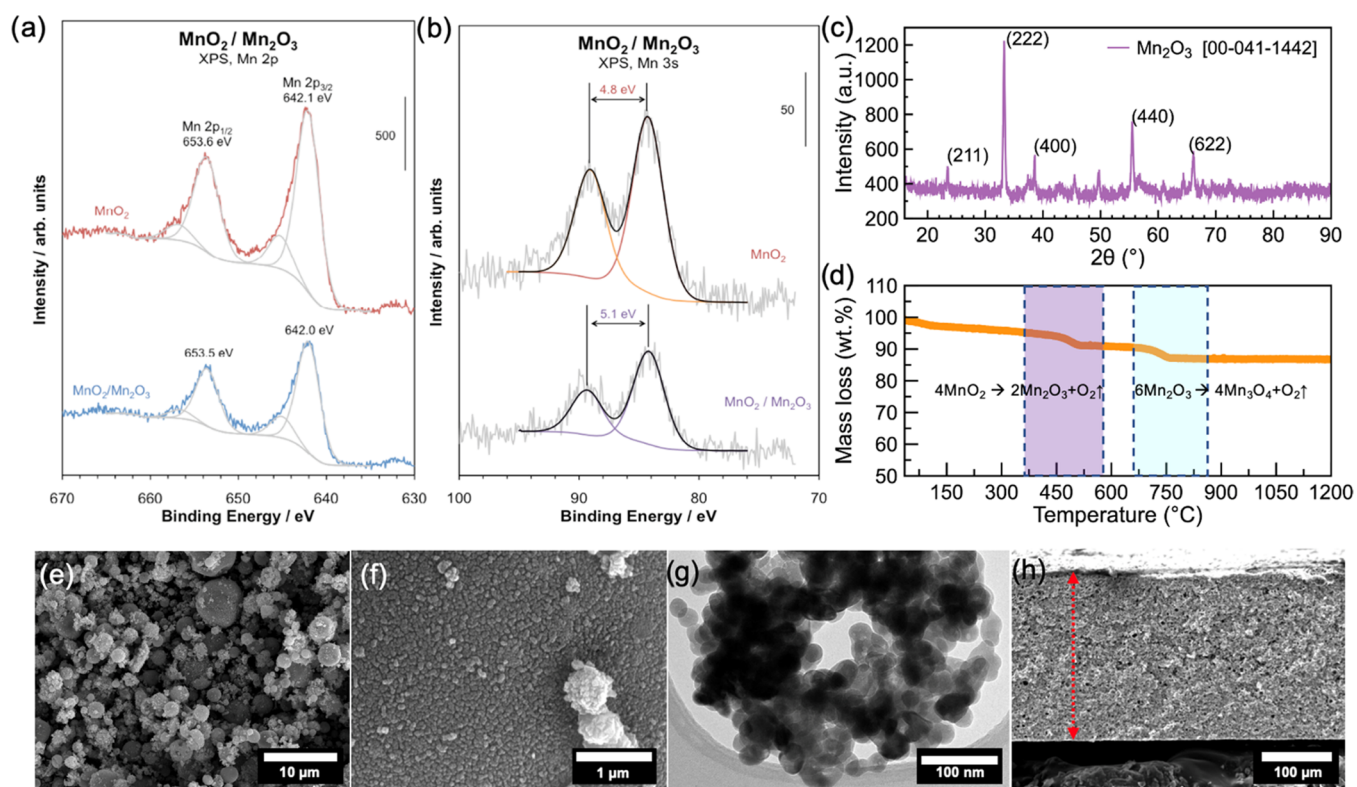|	nAl[43]	Al_2O_3[43]	PVDF[44,45]	MnO_2[46−48]	Mn_2O_3[41,48]
mass density (kg/m^3)	2941	3970	1780	5030	4500
relative permittivity	1	9.6 − 0.0006j	7 − 0.0009j	10.47 − 3.58j	4 − 3j
relative permeability	1	1	1	1.03 − 0.1j	1
electrical conductivity (S/m)	3.75×10^7	1×10^{-14}	1×10^{-10}	5×10^{-14}	1×10^{-12}
specific heat (J/mol K)	900	765	1200	54.1	80
thermal conductivity (W/m K)	237	36	0.19	0.209	0.4

Figure 2. X-ray photoelectron spectroscopy of the as-received manganese oxide powder showing a mixture of MnO_2 and Mn_2O_3: (a) spectrum of 2p peaks, (b) spectrum of 3s peaks, (c) X-ray diffraction analysis of the manganese oxide nanopowder, (d) thermogravimetric analysis of the as-received nanopowder in argon demonstrating phase change from $MnO_2 \rightarrow Mn_2O_3$ and $Mn_2O_3 \rightarrow Mn_3O_4$ and respective O_2 content loss, (e, f) SEM images of the MnO_2/Mn_2O_3 nanopowder, (g) TEM of the nanopowder, and (h) SEM image of the fabricated MnO_2/Mn_2O_3 film at 90 wt % MnO_x loading in the 4 wt % PVDF/6 wt % HPMC matrix.
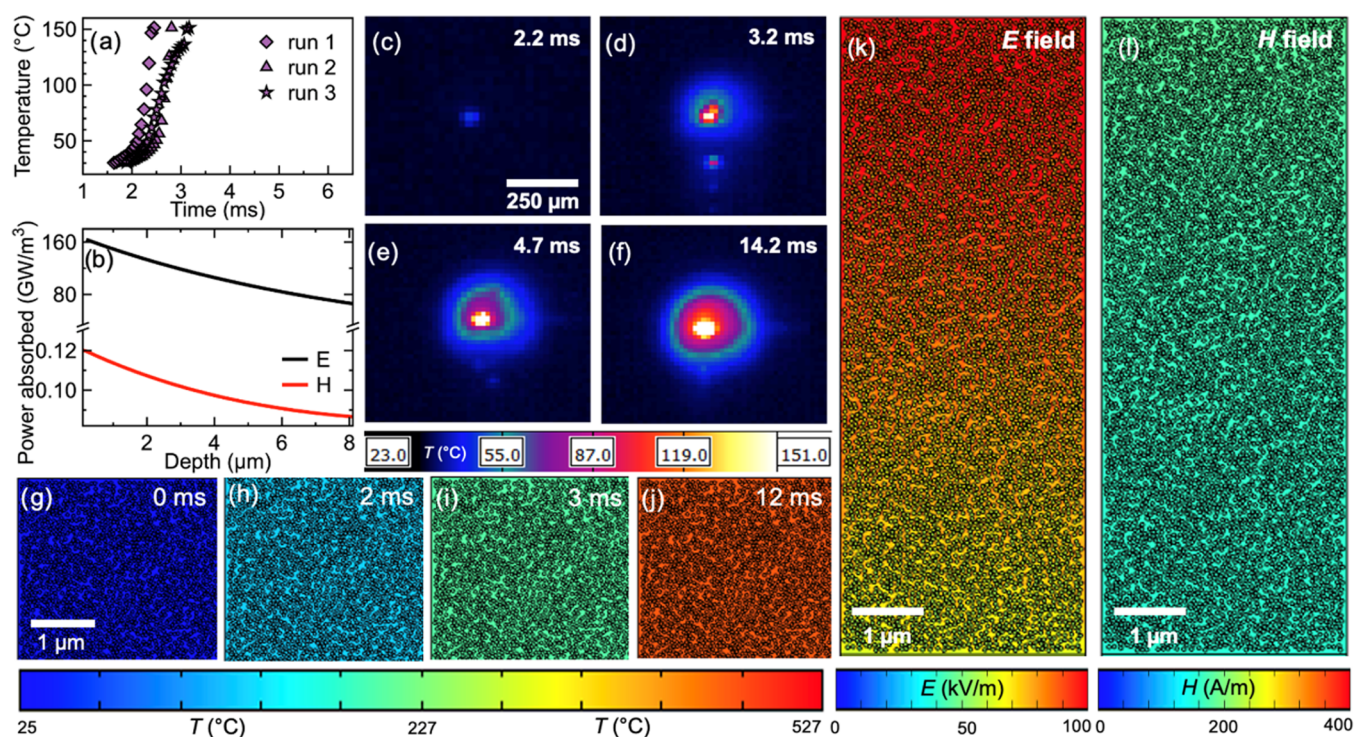

Figure 3. (a) Experimental heating rate from thermal imaging, (b) power absorbed by electric and magnetic field components as a function of film depth from finite element simulation results, (c−f) infrared thermometry snapshots of MnO_2/Mn_2O_3 films, (f−i) finite element simulation results of temperature profiles in the microstructure of the MnO_2/Mn_2O_3 films, (j) electric field profile of the MnO_2/Mn_2O_3 films at $t = 1$ ms, and (k) magnetic field profile in the MnO_2/Mn_2O_3 film at $t = 1$ ms.
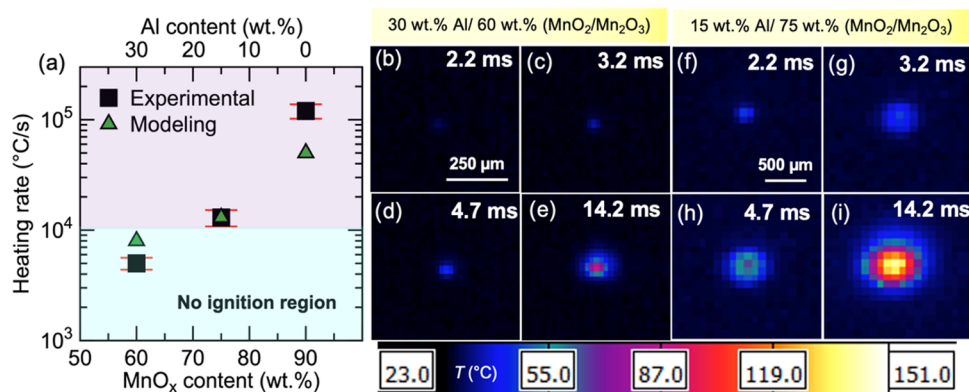
Figure 4. (a) Experimental and simulated microwave heating rates of the films at varying ratios of manganese oxide and nAl and fixed content of the 4 wt % PVDF/6 wt % HPMC binder; infrared thermal images of nAl-based thermite composites at t = 2.2, 3.2, 4.7, and 14.2 ms: (b–e) at 60 wt % loading of MnO_2/Mn_2O_3 and (f–i) at 75 wt % loading of MnO_2/Mn_2O_3.

Calculation of the mass balance eqs 1 and 2 presented below concludes that the as-received powder is a mixture of 40 wt % Mn_2O_3 and 60 wt % MnO_2.

$$4MnO_2 \rightarrow 2Mn_2O_3 + O_2\uparrow \tag{1}$$

$$6Mn_2O_3 \rightarrow 4Mn_3O_4 + O_2\uparrow \tag{2}$$

The particles of MnO_2/Mn_2O_3 have a primary size distribution from 30 to 50 nm (Figure 2f–h) and form nanoparticle clusters in the as-received powders, as shown in Figure 2e,f. For simplicity, the MnO_2/Mn_2O_3 nanoparticles at the 2/3 mass ratio will be referred to as MnO_x in the rest of the paper.

The obtained MnO_x nanopowder was processed into inks at 90 wt % solid loading and printed at a 250 μm thickness, as shown in Figure 2h. The films were tested with the monopole antenna setup at 2.45 GHz incident EM radiation (Figure 1). The infrared camera tests under 15 W of applied microwave power showed that the heating rate of manganese oxide was on the order of 2 × 10^5 °C/s (see Figure 3a). The heating rate of the printed composites was computed in a temperature region below which any exothermic/endothermic chemistry occurs, determined by differential scanning calorimetry (described later). The heating is first localized to a few pixels under the immediate area of the antenna tip. As time progresses, the heated region expands to over 250 μm radial depth (see Figure 3c–f). The initial localization of the heating is due to the higher intensity field present at the antenna tip;[54−56] therefore, the microwave sensitizer was kept in close proximity to the higher microwave intensity zone. The spread of the heated region over the immediate microwave incidence zone is mainly due to heat conduction away from the microwave-sensitized zone, based on the characteristic thermal diffusion times of the assembled films. The finite element simulations of the heating of the film microstructure demonstrate that nanoparticles instantly heat under the incident wavelength and reach thermal equilibrium with the polymer binder surrounding them in ~1 ms. This is due to the instantaneous nature of energy transfer from EM absorption to thermal output.[57] Manganese oxide is nonmagnetic,[40,46,58] and hence, heating of MnO_2/Mn_2O_3 occurs primarily via the electric rather than the magnetic field. This is illustrated in Figure 3b, which shows that the power absorbed by the electric field in the nanoparticles is 3 orders of magnitude higher than that of the magnetic field, where maximum electric field absorption at the film surface is 160 GW/m³ and magnetic field absorption is 0.12 GW/m³. To

understand the effect of nAl loading in microwave heating and ignition of the nAl/MnO_x thermite system, the infrared thermometry of fabricated films was studied at different equivalence ratios.

Since microwave absorption of nAl is negligible,[23,59] one must rely on the manganese oxide sensitizer content, which can be increased to change the heating rate in the films, as demonstrated in Figure 4a both experimentally and via modeling. The heating rates based on the modeling show a similar trend as the experimentally observed values, where MnO_x content decrease is accompanied by lower heating rates. The difference between the experimental and modeled values can be attributed to the inhomogeneous distribution of nanoparticles in the films and limitations of the two-dimensional modeling where heat losses to the environment were not fully encompassed, as described in the experimental section. Additionally, the actual dielectric properties of the MnO_x nanoparticles might differ from the values found in the literature, which were used in the computations. However, the results still depict the microwave incidence effects in the microstructures of the nAl/MnO_x composites. Experimental microwave heating rate increases from 5 × 10^3 to 1.3 × 10^4 °C/s as the content of MnO_x is increased from 60 wt % (equivalence ratio, φ = 0.4) to 75 wt % (equivalence ratio, φ = 1). This range also demarks the ignition threshold with ignition taking place within a 10−100 ms temporal window. Below this threshold level, the exposure times up to 1 min still do not lead to ignition. For the ignition to occur, the rate of energy deposition $\left(\rho c_p \frac{dT}{dt}\right)$ must surpass the energy threshold presented by minimum ignition energy (MIE) presented in eq 3 below

$$\rho c_p \frac{dT}{dt} \geq \frac{MIE}{t_{ign}} \tag{3}$$

$$MIE = \rho c_p(T_{ign} - T_{ambient}) \tag{4}$$

where ρ is the composite density, c_p is the specific heat capacity, $\frac{dT}{dt}$ is the rate of temperature change, T_{ign} is the ignition temperature, $T_{ambient}$ is the ambient temperature, and t_{ign} is the time to ignition. As discussed later in the manuscript sample, heating below 180 °C does not involve any endothermic/exothermic chemistry. Therefore, the external heat generation rate in this region (based upon the values from
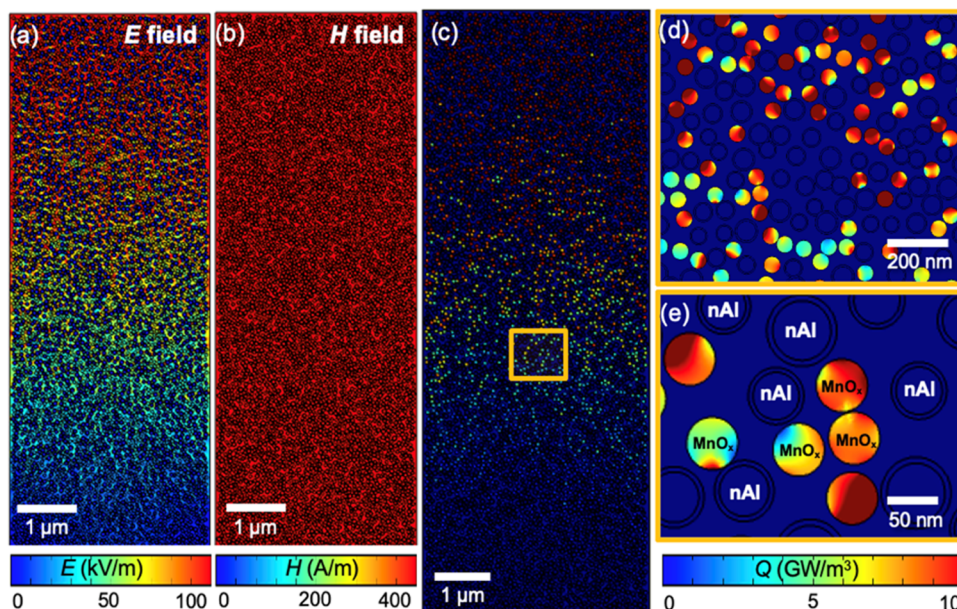
Figure 5. Finite element simulation results of nAl/MnO$_2$/Mn$_2$O$_3$ composites at 75 wt % MnO$_2$/Mn$_2$O$_3$ loading under 2.45 GHz 0.5 MV/m field strength: (a) electric field distribution in the films at t = 4 ns, (b) magnetic field distribution in the films at t = 1 ms, and (c−e) total heat absorbed by the films.
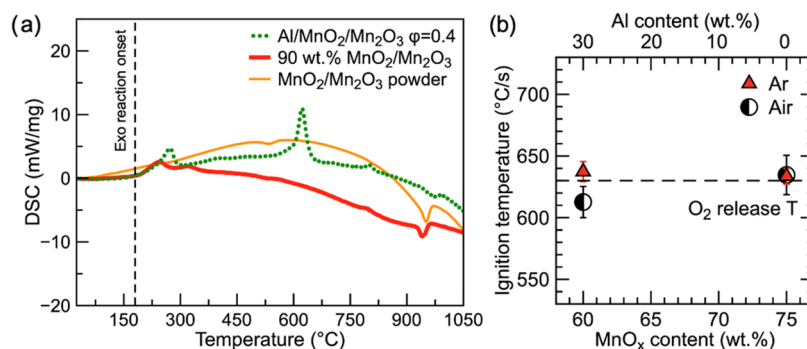

Figure 6. (a) DSC of Al/MnO$_2$/Mn$_2$O$_3$, MnO$_2$/Mn$_2$O$_3$ composites, and MnO$_2$/Mn$_2$O$_3$ nanopowder in air and (b) T-jump ignition results of Al/MnO$_2$/Mn$_2$O$_3$ energetic composites at 60 and 75 wt % MnO$_2$/Mn$_2$O$_3$ loading compared in air and argon.

Figure 4a) is the sole result of the balance between microwave absorption of the composites and the heat losses involved (see eq 5).

$$T < 180 \,^{\circ}\text{C} \rightarrow Q_{\text{chem}} = 0$$

$$\rho c_{\text{p}} \frac{\text{d}T}{\text{d}t} = Q_{\text{abs}} - Q_{\text{lost}} \tag{5}$$

The heat generation rate (left side of eq 5) can be deduced experimentally from the rate of temperature change and material properties (Table 1) to yield 14.4 and 5.6 GW/m^3 for the 75 and 60 wt % samples, respectively. From eq 4, the minimum energy (MIE) required to ignite the sample based on T-jump ignition data was 651 and 676 MJ/m^3 for the φ = 1 and φ = 0.4 samples, respectively. Importantly, the ignition temperatures from T-jump data were selected due to the proximity of the latter to microwave heating rates of 10^3−10^5 °C/s. An estimate of the time to ignition from eq 3 using the experimental power absorbed and the MIE gives a minimum time to ignition in the two samples of 45 and 117 ms. Although this analysis does not consider any exothermicity occurring prior to ignition, the alignment of the minimum estimated time

with the experimentally determined ignition delay times (φ = 0.4 samples) demonstrates that the MW source is acting as a thermal heat source at the particle level and secondary effects such as plasmon resonance and dielectric discharge do not influence the heating prior to ignition. Interestingly, the relation between the sensitizer content and heating rate is nonlinear, where a 15 wt % decrease in the sensitizer content results in a 60% decrease in the heating rate. The simulation results show that $\dot{Q}_{\text{abs model}}$ in φ = 1 and 0.4 samples is 8.5 and 16.8 GW/m^3, respectively, confirming that a 15 wt % increase in MnO$_x$ accounts for doubling in the composite absorption rates. This confirms that the decrease in the sensitizer content can significantly alter the energy deposition rates. As the amount of nAl is increased and the content of MnO$_x$ is decreased to 60 wt %, the films do not reach the ignition temperature. This could mainly be due to (i) reduced overall microwave absorption capability of the composites and (ii) higher thermal conductivity of the films with increased nAl content. A combination of these factors results in a faster heat dissipation away from the irradiance zone that precludes film ignition. These effects can be clearly seen in Figure 4b−i, where at 3.2 ms, the films at φ = 1 have localized heat to a
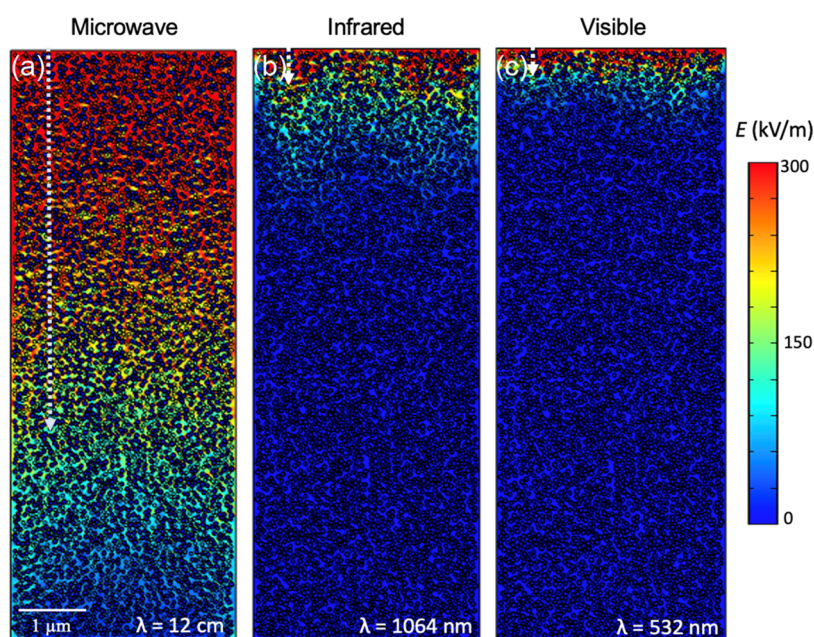
Figure 7. Electric field induced in the matrix of 15 wt % Al/75 wt % (MnO$_2$/Mn$_2$O$_3$) films at incident wavelengths of (a) 12 cm and (b) 1064 nm and (c) 532 nm (from left to right).

radial region of 20 μm, while MnO$_x$-rich samples spanned to the radial region 250 μm. Under incident microwave irradiation, the critical region is getting heated but is also losing the gained heat to the surrounding microstructure and the supported film is mounted on via conduction as well as convection. The higher rate of heat transfer in samples with the increased nAl content results in faster heat dissipation and a rapid approach to a steady-state temperature (i.e., no ignition).

Finite element simulations of the nAl/MnO$_x$ mixtures show that manganese oxide nanoparticles heat first under the incident wavelength and transfer heat to the neighboring aluminum nanoparticles and the polymer binder (see Figure 5a−e). Manganese oxide accounts for 99.4% of the absorption in the assembled energetic films and negligible absorption by nAl particles is seen. The volumetric power absorbed by MnO$_x$ nanoparticles is in the range of 5−10 GW/m^3, which gives the total heat absorbed per MnO$_x$ nanoparticle of 0.7 pW. Compared to absorption with other microwave sensitizers, such as nTi, the absorption of MnO$_x$ particles is 2 orders of magnitude lower than nTi,[20] which also leads to a much longer ignition delay time for MnO$_x$. To better understand the thermochemistry in fabricated nAl/MnO$_x$ thermites, differential scanning calorimetry and T-jump ignition tests were conducted.

As mentioned earlier, manganese dioxide undergoes a two-step phase change process that is accompanied by mass loss due to O$_2$ release (see eqs 1 and 2). Both of the phase change steps to Mn$_2$O$_3$ and Mn$_3$O$_4$ under air flow are endothermic and occur at 530 and 920 °C, respectively, as confirmed by DSC data in Figure 6a. Interestingly, the second endotherm occurs at a higher temperature in air than was detected in an argon environment in Figure 2d.[60] When fabricated into a polymer binder, both MnO$_x$ and nAl/MnO$_x$ composites do not undergo any endothermic/exothermic chemistry below 180 °C. The first exotherm in the DSC plot is characteristic of exothermic decomposition of the polymer binder[61,62] with corresponding peaks at 240 and 270 °C for MnO$_x$ and nAl/MnO$_x$ composites, respectively. The mass loss from MnO$_x$/

HPMC/PVDF films confirms that MnO$_2$ releases O$_2$ at 530 °C, which is shortly followed by the exothermic reaction with Al.[63,64] These results are further confirmed by ultrafast heating temperature jump ignition and mass spectrometry results presented in Figure 6b. Both ignitions in air and argon environments occur after O$_2$ release from MnO$_x$ at 620 °C. The difference in O$_2$ release temperatures in DSC and T-jump ignition data is due to the 10^4 order of magnitude difference in heating rates.[65,66] The heating rate in T-jump experiments is at the order of 10^5 °C/s, which is closer to the observed heating rates under microwave stimulation. Numerous studies reported that oxidation of nAl proceeds when the passivating shell is compromised due to polymorphic phase changes in Al$_2$O$_3$ and diffusion of Al cations and O$_2$ species drives ignition.[67,68] Our results imply that the heat transfer from MnO$_x$ particles, localized heating of nAl particles, and O$_2$ release from the oxidizer allow the ignition to occur under microwave irradiation. X-ray diffraction analysis on post-product species in air (Figure S1) showed traces of galaxite formation (MnAl$_2$O$_4$) with no traces of remnant Al, implying full consumption of the metal fuel in the reaction.

When stimulated under EM radiation, a significant factor to consider alongside microwave sensitizer content and thermochemistry that drive ignition is an energy deposition depth of the incident wave into the material volume. Finite element simulation of the films in Figure 7 shows that under electromagnetic stimulation at 2.45 GHz (λ = 12 cm), 564 THz (λ = 532 nm), and 282 THz (λ = 1062 nm), the nanoparticles absorb more effectively at higher-energy frequencies, leading to a shorter penetration depth. Although 3D printed nAl/MnO$_x$ composites are comprised of nanoscale constituents that have skin depths larger than their size, their assembly into microstructures at 90 wt % nanoparticle loading enables percolating pathways within the macrostructure.[69,70] This in turn introduces a screening of the incident wavelength and the wave interaction only within the assembled microstructure's penetration depth. Penetration depth is defined as a distance where the maximum amplitude of the incident wave

decays by 63%, as it propagates into the material.[57] As seen in eq 6, penetration depth in conductive materials (δ) is inversely proportional to the incident frequency (f), permeability of free space (μ_0), magnetic permeability (μ), and electrical conductivity (σ) of the sample under test. Considering the mass averaged electrical conductivity (Table 1) of nAl, MnO$_x$, and the polymers, the penetration depth of the films at the 15 wt % nAl content was calculated at each simulated frequency based on eq 6.

$$\delta = \sqrt{\frac{2}{2\pi f \mu_0 \mu \sigma}} \tag{6}$$

As such, penetration depths based on the macroscopic electrical conductivity of the composites were 6.7 μm, 22 nm, and 16 nm at 2.45 GHz, 282 THz, and 564 THz, respectively. Unlike IR and visible ignition sources where absorption at high solids loading is limited to nanoscale depth heating, microwave absorption is not limited by a narrow penetration depth for conductive composites. Figure 7a demonstrates the heating in the printed samples under incident radiation at 2.45 GHz where the deposited electric field drops with the depth of the film from a maximum value of 300 kV/m to about 110 kV/m in 6 μm. In contrast, at 532 and 1064 nm, the electric field decreases rapidly within the nanometer scale and no electric field can be deposited beyond 500 nm depth (see Figure 7b,c). Furthermore, and from a practical standpoint, the ability to print suggests the ability to embed MW sensitizers within the body of a structure to initiate chemistry in the desired location.

4. CONCLUSIONS

This work demonstrates that ignition of nAl/MnO$_x$ energetic composites can be modulated via microwave energy without the addition of electromagnetic sensitizers that do not participate in the energetic reaction. The mechanism of nanoscale Al/MnO$_x$ ignition under EM stimulation at 2.45 GHz was studied at different oxidizer loadings. The experimental infrared thermometry coupled with finite element simulations showed that MnO$_x$ nanoparticles effectively heat under microwave irradiation via electric field absorption and transfer heat to the surrounding Al nanoparticles. In situ TOFMS T-jump ignition results revealed that O$_2$ release temperature from MnO$_2$, present in the oxidizer, coincides with the ignition in the energetic composites of nAl/MnO$_x$. These results demonstrate that MnO$_x$ nanoparticles transfer heat to the surrounding media and undergo O$_2$ release creating favorable conditions for nAl oxidation due to incident microwave energy. The longer wavelength of the incident microwave energy as opposed to infrared or visible energy sources allows deeper penetration of the incident wave into the composite volume. The results presented here demonstrate that 3D printed microwave-sensitive energetic composites can be used to initiate chemistry in desired locations within material volumes and may play a vital role in controlling energy release pathways in energetic materials.

ASSOCIATED CONTENT

Ⓢ Supporting Information

The Supporting Information is available free of charge at https://pubs.acs.org/doi/10.1021/acsanm.1c04157.

X-ray diffraction analysis results on the reaction post-products (PDF)

AUTHOR INFORMATION

Corresponding Author

Michael R. Zachariah − *Materials Science and Engineering Program, University of California, Riverside, California 92521, United States; Department of Chemical and Environmental Engineering, University of California, Riverside, California 92521, United States; Department of Chemistry and Biochemistry, University of Maryland, College Park, Maryland 20742, United States;* ⓘ orcid.org/0000-0002-4115-3324; Email: mrz@engr.ucr.edu

Authors

Zaira Alibay − *Materials Science and Engineering Program, University of California, Riverside, California 92521, United States;* ⓘ orcid.org/0000-0002-1335-9202

Daniel Olsen − *School of Mechanical Engineering, Georgia Institute of Technology, Atlanta, Georgia 30313, United States*

Prithwish Biswas − *Department of Chemical and Environmental Engineering, University of California, Riverside, California 92521, United States;* ⓘ orcid.org/0000-0002-9921-2905

Cody England − *Chemical and Biomolecular Engineering Department, University of California, Los Angeles, California 90095, United States*

Feiyu Xu − *Department of Chemistry and Biochemistry, University of Maryland, College Park, Maryland 20742, United States*

Pankaj Ghildiyal − *Department of Chemistry and Biochemistry, University of Maryland, College Park, Maryland 20742, United States;* ⓘ orcid.org/0000-0002-4422-3068

Min Zhou − *School of Mechanical Engineering, Georgia Institute of Technology, Atlanta, Georgia 30313, United States*

Complete contact information is available at:
https://pubs.acs.org/10.1021/acsanm.1c04157

Notes

The authors declare no competing financial interest.

REFERENCES

(1) Wang, L.; Munir, Z.; Maximov, Y. Review of Thermite Reactions. *J. Mater. Sci.* **1993**, 28, 3693−3708.

(2) Weismiller, M. R.; Malchi, J. Y.; Lee, J. G.; Yetter, R. A.; Foley, T. J. Effects of Fuel and Oxidizer Particle Dimensions on the Propagation of Aluminum Containing Thermites. *Proc. Combust. Inst.* **2011**, 33, 1989−1996.

(3) Koenig, J. T.; Shaw, A. P.; Poret, J. C.; Eck, W. S.; Groven, L. J. Performance of W/MnO2 as an Environmentally Friendly Energetic Time Delay Composition. *ACS Sustainable Chem. Eng.* **2017**, 5, 9477−9484.

(4) Pantoya, M. L.; Granier, J. J. Combustion Behavior of Highly Energetic Thermites: Nano versus Micron Composites. *Propellants, Explos., Pyrotech.* **2005**, *30*, 53−62.

(5) Aumann, C. E.; Skofronick, G. L.; Martin, J. A. Oxidation Behavior of Aluminum Nanopowders. *J. Vac. Sci. Technol., B: Microelectron. Nanometer Struct.–Process., Meas., Phenom.* **1995**, *13*, 1178−1183.

(6) Rossi, C. Two Decades of Research on Nano-Energetic Materials. *Propellants, Explos., Pyrotech.* **2014**, *39*, 323−327.

(7) Wang, H.; Jian, G.; Yan, S.; Delisio, J. B.; Huang, C.; Zachariah, M. R. Electrospray Formation of Gelled Nano-Aluminum Microspheres with Superior Reactivity. *ACS Appl. Mater. Interfaces* **2013**, *5*, 6797−6801.

(8) Wang, H.; Kline, D. J.; Rehwoldt, M.; Wu, T.; Zhao, W.; Wang, X.; Zachariah, M. R. Architecture Can Significantly Alter the Energy Release Rate from Nanocomposite Energetics. *ACS Appl. Polym. Mater.* **2019**, *1*, 982−989.

(9) Calais, T.; Bancaud, A.; Estève, A.; Rossi, C. Correlation between DNA Self-Assembly Kinetics, Microstructure, and Thermal Properties of Tunable Highly Energetic Al-CuO Nanocomposites for Micropyrotechnic Applications. *ACS Appl. Nano Mater.* **2018**, *1*, 4716−4725.

(10) Arkhipov, V. A.; Korotkikh, A. G. The Influence of Aluminum Powder Dispersity on Composite Solid Propellants Ignitability by Laser Radiation. *Combust. Flame* **2012**, *159*, 409−415.

(11) Bourne, N. K. On the Laser Ignition and Initiation of Explosives. *Proc. R. Soc. A* **2001**, *457*, 1401−1426.

(12) Huang, S.; Parimi, V. S.; Deng, S.; Lingamneni, S.; Zheng, X. Facile Thermal and Optical Ignition of Silicon Nanoparticles and Micron Particles. *Nano Lett.* **2017**, *17*, 5925−5930.

(13) Agrawal, D. K. Microwave Processing of Ceramics. *Curr. Opin. Solid State Mater. Sci.* **1998**, *3*, 480−485.

(14) Sutton, W. H. Microwave Processing of Materials. *MRS Bull.* **1993**, *18*, 22−29.

(15) Fang, X.; R Ahmad, S. Laser Ignitability of Insensitive Propellants. *Adv. Mater. Sci* **2018**, *3*, 1−4.

(16) Ahmad, S. R.; Russell, D. A. Laser Ignition of Pyrotechnics - Effects of Wavelength, Composition and Confinement. *Propellants, Explos., Pyrotech.* **2005**, *30*, 131−139.

(17) Uhlenhake, K. E.; Olsen, D.; Gomez, M.; Örnek, M.; Zhou, M.; Son, S. F. Photoflash and Laser Ignition of Full Density Nano-Aluminum PVDF Films. *Combust. Flame* **2021**, *233*, No. 111570.

(18) Barkley, S. J.; Zhu, K.; Lynch, J. E.; Michael, J. B.; Sippel, T. R. Microwave Plasma Enhancement of Multiphase Flames: On-Demand Control of Solid Propellant Burning Rate. *Combust. Flame* **2019**, *199*, 14−23.

(19) Zhu, K.; Barkley, S. J.; Sippel, T. R.; Michael, J. B. Flame Temperature Characterization of Microwave-Assisted Aluminum Particle Combustion. *AIAA Scitech 2019 Forum* **2019**, 1−10.

(20) Alibay, Z.; Kline, D. J.; Rehwoldt, M. C.; Biswas, P.; Herrera, S.; Wang, H.; Zachariah, M. R. Mechanism of Microwave-Initiated Ignition of Sensitized Energetic Nanocomposites. *Chem. Eng. J.* **2021**, *415*, No. 128657.

(21) Porch, A.; Slocombe, D.; Edwards, P. P. Microwave Absorption in Powders of Small Conducting Particles for Heating Applications. *Phys. Chem. Chem. Phys.* **2013**, *15*, 2757−2763.

(22) Biswas, P.; Mulholland, G. W.; Rehwoldt, M. C.; Kline, D. J.; Zachariah, M. R. Microwave Absorption by Small Dielectric and Semi-Conductor Coated Metal Particles. *J. Quant. Spectrosc. Radiat. Transfer* **2020**, *247*, No. 106938.

(23) Kline, D. J.; Rehwoldt, M. C.; Turner, C. J.; Biswas, P.; Mulholland, G. W.; Mcdonnell, S. M.; Zachariah, M. R. Spatially Focused Microwave Ignition of Metallized Energetic Materials. *J. Appl. Phys.* **2020**, *127*, No. 055901.

(24) Sanders, V. E.; Asay, B. W.; Foley, T. J.; Tappan, B. C.; Pacheco, A. N.; Son, S. F. Reaction Propagation of Four Nanoscale Energetic Composites (Al/MoO3, Al/WO3, Al/CuO, and B12O3). *J. Propul. Power* **2007**, *23*, 707−714.

(25) Granier, J. J.; Plantier, K. B.; Pantoya, M. L. The Role of the Al2O3 Passivation Shell Surrounding Nano-Al Particles in the Combustion Synthesis of NiAl. *J. Mater. Sci.* **2004**, *39*, 6421−6431.

(26) Comet, M.; Martin, C.; Schnell, F.; Spitzer, D. Nanothermites: A Short Review. Factsheet for Experimenters, Present and Future Challenges. *Propellants, Explos., Pyrotech.* **2019**, *44*, 18−36.

(27) Fischer, S.; Grubelich, M. In *Theoretical Energy Release of Thermites, Intermetallics, and Combustible Metals*, 24th International Pyrotechnics Seminar, 1998; Vol. *220*, 56.

(28) Jian, G.; Piekiel, N. W.; Zachariah, M. R. Time-Resolved Mass Spectrometry of Nano-Al and Nano-Al/CuO Thermite under Rapid Heating: A Mechanistic Study. *J. Phys. Chem. C* **2012**, *116*, 26881−26887.

(29) Crane, C. A.; Pantoya, M. L.; Weeks, B. L. Investigating the Trade-Offs of Microwave Susceptors in Energetic Composites: Microwave Heating versus Combustion Performance. *J. Appl. Phys.* **2014**, *115*, No. 104106.

(30) Meir, Y.; Jerby, E. Localized Rapid Heating by Low-Power Solid-State Microwave Drill. *IEEE Trans. Microwave Theory Tech.* **2012**, *60*, 2665−2672.

(31) Vargas, E.; Pantoya, M. L.; Saed, M. A.; Weeks, B. L. Advanced Susceptors for Microwave Heating of Energetic Materials. *Mater. Des.* **2016**, *90*, 47−53.

(32) Barkley, S. J.; Lawrence, A. R.; Zohair, M.; Smithhisler, O. L.; Pint, C. L.; Michael, J. B.; Sippel, T. R. Smart Electromagnetic Thermites: GO/RGO Nanoscale Thermite Composites with Thermally Switchable Microwave Ignitability. *ACS Appl. Mater. Interfaces* **2021**, *13*, 39678−39688.

(33) Jiaxing, S.; Tao, G.; Wen, D.; Yiming, M.; Xiang, F.; Hao, W. In *Study on Thermal Chemical Reaction of Al/MnO2 Thermite*, IOP Conference Series: Earth and Environmental Science, 2018; p 186.

(34) Song, J.; Guo, T.; Yao, M.; Chen, J.; Ding, W.; Bei, F.; Mao, Y.; Yu, Z.; Huang, J.; Zhang, X.; et al. A Comparative Study of Thermal Kinetics and Combustion Performance of Al/CuO, Al/Fe2O3 and Al/MnO2 Nanothermites. *Vacuum* **2020**, *176*, No. 109339.

(35) Song, J.; Guo, T.; Ding, W.; Yao, M.; Yang, L.; Zhang, X.; Yu, Z.; Wu, J.; Zhang, J.; Fang, X. The Effect of Al Particles Size on the Thermal Behavior and Kinetics of Al-MnO2 Thermite System. *Adv. Mater. Sci. Eng.* **2020**, *2020*, 1−11.

(36) Baghurst, D. R.; Mingos, D. M. P. Application of Microwave Heating Techniques for the Synthesis of Solid State Inorganic Compounds. *J. Chem. Soc. Chem. Commun.* **1988**, *12*, 829−830.

(37) Vileno, E.; Zhou, H.; Zhang, Q.; Suib, S. L.; Corbin, D. R.; Koch, T. A. Synthetic Todorokite Produced by Microwave Heating: An Active Oxidation Catalyst. *J. Catal.* **1999**, *187*, 285−297.

(38) Marún, C.; Conde, L. D.; Suib, S. L. Catalytic Oligomerization of Methane via Microwave Heating. *J. Phys. Chem. A* **1999**, *103*, 4332−4340.

(39) Wang, X.; Lv, G.; Liao, L.; Wang, G. Manganese Oxide - an Excellent Microwave Absorbent for the Oxidation of Methylene Blue. *RSC Adv.* **2015**, *5*, 55595−55601.

(40) Guan, H.; Liu, S.; Zhao, Y.; Duan, Y. Electromagnetic Characteristics of Nanometer Manganese Dioxide Composite Materials. *J. Electron. Mater* **2006**, *35*, 892−896.

(41) Duan, Y.; Liu, Z.; Jing, H.; Yin, K.; Liu, S. The Effects of Annealing Treatment on the Morphology and Microwave Absorption Properties of α-MnO2. *Proc. Inst. Mech. Eng., Part L* **2013**, *227*, 61−69.

(42) COMSOL Multiphysics. Stockholm.

(43) Crane, C. A.; Pantoya, M. L.; Weeks, B. L.; Saed, M. The Effects of Particle Size on Microwave Heating of Metal and Metal Oxide Powders. *Powder Technol.* **2014**, *256*, 113−117.

(44) Zhou, W.; Zuo, J.; Ren, W. Thermal Conductivity and Dielectric Properties of Al/PVDF Composites. *Composites, Part A* **2012**, *43*, 658−664.

(45) Meng, X. M.; Zhang, X. J.; Lu, C.; Pan, Y. F.; Wang, G. S. Enhanced Absorbing Properties of Three-Phase Composites Based on a Thermoplastic-Ceramic Matrix (BaTiO3 + PVDF) and Carbon Black Nanoparticles. *J. Mater. Chem. A* **2014**, *2*, 18725−18730.

(46) Yuping, D.; He, M.; Xiaogang, L.; Shunhua, L.; Zhijiang, J. The Microwave Electromagnetic Characteristics of Manganese Dioxide with Different Crystallographic Structures. *Phys. B* **2010**, *405*, 1826−1831.

(47) Hedden, M.; Francis, N.; Haraldsen, J. T.; Ahmed, T.; Constantin, C. Thermoelectric Properties of Nano-Meso-Micro *β*-MnO2 Powders as a Function of Electrical Resistance. *Nanoscale Res. Lett.* **2015**, *10*, No. 292.

(48) Jacob, K. T.; Kumar, A.; Rajitha, G.; Waseda, Y. Thermodynamic Data for Mn 3O 4, Mn 2O 3 and MnO 2. *High Temp. Mater. Processes* **2011**, *30*, 459−472.

(49) Zhou, L.; Piekiel, N.; Chowdhury, S.; Zachariah, M. R. Time-Resolved Mass Spectrometry of the Exothermic Reaction between Nanoaluminum and Metal Oxides: The Role of Oxygen Release. *J. Phys. Chem. C* **2010**, *114*, 14269−14275.

(50) Falub, M. C.; Kuepper, K. X-Ray Photoelectron Spectra of Manganites Were Studied. It Was Shown That for the Formal Valence of Manganese from 3+ to 3.3+, the Doping Holes Are O2, 2008, *49*, 54−58.

(51) Galakhov, V. R.; Demeter, M.; Bartkowski, S.; Neumann, M.; Ovechkina, N. A.; Kurmaev, E. Z.; Lobachevskaya, N. I.; Mukovskii, Y. M.; Mitchell, J.; Ederer, D. L. Mn (Formula Presented) Exchange Splitting in Mixed-Valence Manganites. *Phys. Rev. B* **2002**, *65*, No. 113102.

(52) Kochur, A. G.; Kozakov, A. T.; Nikolskii, A. V.; Googlev, K. A.; Pavlenko, A. V.; Verbenko, I. A.; Reznichenko, L. A.; Krasnenko, T. I. Valence State of the Manganese Ions in Mixed-Valence La 1-ABi BMn 1+*δ*O 3±*γ* Ceramics by Mn 2p and Mn 3s X-Ray Photoelectron Spectra. *J. Electron Spectrosc. Relat. Phenom.* **2012**, *185*, 175−183.

(53) Reyes, I. A.; Flores, M.; Palacios, E. G.; Islas, H.; Juárez, J. C.; Reyes, M.; Teja, A. M.; Pérez, C. A. Kinetics of the Thermal Decomposition of Rhodochrosite. *Minerals* **2021**, *11*, No. 34.

(54) Jerby, E.; Dikhtyar, V.; AKTUSHEV, O.; GROSGLICK, U. The Microwave Drill. *Science* **2002**, *298*, 587−589.

(55) Jerby, E.; Aktushev, O.; Dikhtyar, V. Theoretical Analysis of the Microwave-Drill near-Field Localized Heating Effect. *J. Appl. Phys.* **2005**, *97*, No. 034909.

(56) Meir, Y.; Jerby, E. Thermite Powder Ignition by Localized Microwaves. *Combust. Flame* **2012**, *159*, 2474−2479.

(57) Horikoshi, S.; Schiffmann, R. F.; Fukushima, J.; Serpone, N. *Microwave Chemical and Materials Processing: A Tutorial*; Springer, 2018.

(58) Zhang, J.; Yuping, D.; Shuqing, L.; Xiaogang, L.; Shunhua, L. The Effects of High Magnetic Field on the Morphology and Microwave Electromagnetic Properties of MnO2 Powder. *J. Solid State Chem.* **2010**, *183*, 1490−1495.

(59) Rybakov, K. I.; Semenov, V. E.; Egorov, S. V.; Eremeev, A. G.; Plotnikov, I. V.; Bykov, Y. V. Microwave Heating of Conductive Powder Materials. *J. Appl. Phys.* **2006**, *99*, No. 023506.

(60) Tinsley, D. M.; Sharp, J. H. Thermal Analysis of Manganese Dioxide in Controlled Atmospheres. *J. Therm. Anal.* **1971**, *3*, 43−48.

(61) Li, X. G.; Huang, M. R.; Bai, H. Thermal Decomposition of Cellulose Ethers. *J. Appl. Polym. Sci.* **1999**, *73*, 2927−2936.

(62) Delisio, J. B.; Hu, X.; Wu, T.; Egan, G. C.; Young, G.; Zachariah, M. R. Probing the Reaction Mechanism of Aluminum/Poly(Vinylidene Fluoride) Composites. *J. Phys. Chem. B* **2016**, *120*, 5534−5542.

(63) Zhang, J.; Huang, J.; Fang, X.; Li, Y.; Yu, Z.; Gao, Z.; Wu, S.; Yang, L.; Wu, J.; Kui, J. Thermal Decomposition and Thermal Reaction Process of PTFE/Al/MnO2 Fluorinated Thermite. *Materials* **2018**, *11*, No. 2451.

(64) Song, J.; Guo, T.; Ding, W.; Yao, M.; Bei, F.; Zhang, X.; Huang, J.; Fang, X. Study on Thermal Behavior and Kinetics of Al/MnO2 Poly(Vinylidene Fluorine) Energetic Nanocomposite Assembled by Electrospray. *RSC Adv.* **2019**, *9*, 25266−25273.

(65) Williams, R. A.; Patel, J. V.; Ermoline, A.; Schoenitz, M.; Dreizin, E. L. Correlation of Optical Emission and Pressure Generated upon Ignition of Fully-Dense Nanocomposite Thermite Powders. *Combust. Flame* **2013**, *160*, 734−741.

(66) Jian, G.; Zhou, L.; Piekiel, N. W.; Zachariah, M. R. Low Effective Activation Energies for Oxygen Release from Metal Oxides: Evidence for Mass-Transfer Limits at High Heating Rates. *ChemPhysChem* **2014**, *15*, 1666−1672.

(67) Trunov, M. A.; Schoenitz, M.; Dreizin, E. L. Effect of Polymorphic Phase Transformations in Alumina Layer on Ignition of Aluminium Particles. *Combust. Theory Modell.* **2006**, *10*, 603−623.

(68) Chowdhury, S.; Sullivan, K.; Piekiel, N.; Zhou, L.; Zachariah, M. R. Diffusive vs Explosive Reaction at the Nanoscale. *J. Phys. Chem. C* **2010**, *114*, 9191−9195.

(69) Yang, L.; Zhao, Q.; Hou, Y.; Sun, R.; Cheng, M.; Shen, M.; Zeng, S.; Ji, H.; Qiu, J. High Breakdown Strength and Outstanding Piezoelectric Performance in Flexible PVDF Based Percolative Nanocomposites through the Synergistic Effect of Topological-Structure and Composition Modulations. *Composites, Part A* **2018**, *114*, 13−20.

(70) Zhang, L.; Wang, W.; Wang, X.; Bass, P.; Cheng, Z. Y. Metal-Polymer Nanocomposites with High Percolation Threshold and High Dielectric Constant. *Appl. Phys. Lett* **2013**, *103*, No. 232903.

☐ Recommended by ACS

In-Situ Thermochemical Shock-Induced Stress at the Metal/Oxide Interface Enhances Reactivity of Aluminum Nanoparticles

Prithwish Biswas, Michael R. Zachariah, *et al.*

JUNE 06, 2022
ACS APPLIED MATERIALS & INTERFACES   READ ☑

Molecular Dynamics Insight into the Evolution of Al Nanoparticles in the Thermal Decomposition of Energetic Materials

Weizhe Hao, Chaoyang Zhang, *et al.*

APRIL 27, 2020
THE JOURNAL OF PHYSICAL CHEMISTRY C   READ ☑

Oxidation of Aluminum Particles from 1 to 10 nm in Diameter: The Transition from Clusters to Nanoparticles

Kyle R. Overdeep, C. Michael Lindsay, *et al.*

SEPTEMBER 13, 2019
THE JOURNAL OF PHYSICAL CHEMISTRY C   READ ☑

Engineered Porosity-Induced Burn Rate Enhancement in Dense Al/CuO Nanothermites

Tao Wu, Carole Rossi, *et al.*

FEBRUARY 22, 2022
ACS APPLIED ENERGY MATERIALS   READ ☑

Get More Suggestions >